International Journal of Solids and Structures 58 (2015) 353–365

Contents lists available at ScienceDirect

International Journal of Solids and Structures

journal homepage: www.elsevier.com/locate/ijsolstr

Analytical solutions for bonded elastically compressible layers

Shutao Qiao, Nanshu Lu *

Center for Mechanics of Solids, Structures and Materials, Department of Aerospace Engineering and Engineering Mechanics, Texas Materials Institute, NASCENT Center, The University of Texas at Austin, Austin, TX 78712, USA

ARTICLE INFO

Article history:
Received 20 April 2014
Received in revised form 13 November 2014
Available online 17 December 2014

Keywords:
Compression
Elastic layer
Effective modulus
Poisson's ratio

ABSTRACT

Compression of elastic layers bonded between parallel plates often find applications in the mechanical characterization of soft materials or the transfer-printing of nanomembranes with polymeric stamps. In addition, annular rubbery gaskets and sealers are often under uniaxial compression during service. Analysis of elastic layers under compression has been focused on nearly incompressible materials such as rubbers, and empirical assumptions of displacements were adopted for simplicity. For compressible materials, solutions obtained by the method of averaged equilibrium are sufficient for effective compression modulus but inaccurate for the displacement or stress fields whereas solutions obtained by the method of series expansion are considerably complicated. In this paper, we report full field, closed-form solutions for bonded elastic layers (disks, annuli, annuli with rigid shafts, infinitely long strips) in compression using separation of variables without any pre-assumed deformation profile. These solutions can satisfy the exact forms of the equilibrium equations and all essential boundary conditions as well as the weak form of the natural boundary conditions. Therefore the predicted stress, displacement, and effective modulus have found excellent agreement with finite element modeling (FEM) results over a wide range of Poisson's ratio and aspect ratio. The analytical and FEM results of the stress, displacement, and effective modulus are highly sensitive to Poisson's ratio, especially near 0.5. Therefore we also propose a viable means to simultaneously measure the intrinsic Young's modulus and Poisson's ratio of elastically compressible layers without camera settings. When Poisson's ratio approaches 0.5, our solutions can degenerate to classical solutions for incompressible elastic layers.

1. Introduction

Elastic layers have found wide engineering applications. For example, rubbery disks and annuli are widely used in industry as gaskets, sealers, and dampers for various machineries. Their material properties are often characterized by uniaxial compression between two parallel plates. It is also easier to measure the elastic properties of soft and fragile materials like hydrogel using compression tests rather than tension tests (Zhao et al., 2010). The effective compression modulus E_c which is also known as the apparent stiffness is defined as the slope of the engineering stress–strain curve. It has been found that E_c is often higher than the intrinsic Young's modulus of the material due to the constraint of the parallel plates which are fully bonded to the elastic layer, i.e. no slippage on the layer-plate interface (Gent and Lindley, 1959). A major mechanics problem is how to accurately relate the load and displacement measurements to the intrinsic elastic properties of the material – the Young's modulus and the Poisson's ratio. Therefore, a simple, analytical solution of elastic layers under uniaxial compression is in need. Besides, full field elastic solutions also serve as the fundamentals for the reliability and failure analysis when the elastic layers are subjected to constant or cyclic compressive forces during services (Kakavas, 1997). Compression of elastic layers can also be found in microfabrication. For instance, elastomeric stamps are widely used in the transfer-printing of nanowires (Lee et al., 2010), nanoribbons (Khang et al., 2006) and nanomembranes (Kim et al., 2008) due to their moldability and appropriate surface adhesion. When the stamp is compressed between a rigid backing layer and the nanomaterials on a rigid donor wafer, the deformation of the stamp and the shear stress on the stamp-nanomaterial interface will dictate the quality of the transfer-printing, i.e. whether the nanomaterials will suffer any transfer-induced wrinkling or cracking. Stresses at the stamp-nanomaterial interface are hence critical information for the failure analysis of the nanomaterials during the transfer-printing process.

Elastic layers in compression have been studied for decades both experimentally and theoretically for different geometries. Series expansion with prescribed displacements (Brady, 1971a,b)

* Corresponding author. Tel.: +1 512 471 4208.
E-mail address: nanshulu@utexas.edu (N. Lu).

http://dx.doi.org/10.1016/j.ijsolstr.2014.11.018
0020-7683/

and energy methods with prescribed stress (Williams et al., 1961) have been employed to obtain analytical solutions. Al-Chalabi and Huang have proposed a stress function (Al-Chalabi and Huang, 1974; Al-Chalabi et al., 1974) to solve for a rubber disks under arbitrary boundary conditions (BCs). Instead of infinite series expansion or sophisticated stress functions, approximate solutions such as the Gent's solution (Gent and Lindley, 1959; Gent and Meinecke, 1970) started to tackle the problem by assuming the sidewall of the elastic disk is deformed in parabolic shape. The Gent's solution captures the behaviors of incompressible materials like polydimethylsiloxane (PDMS) rubber (Wypych, 2012) reasonably well and has therefore been widely used in engineering designs and experiments due to the simplicity. In practice, however, many other polymers like polyimide (PI) have Poisson's ratios ranging from 0.34 to 0.45 (Wilson et al., 1990) and solutions for compressible elastic layers are also important. A "pressure method" has been proposed to seek for approximate solutions to elastically compressible layers. As summarized by Pinarbasi (Pinarbasi et al., 2008), three basic assumptions were commonly adopted in the pressure method: (i) horizontal plane sections remain planar after deformation, (ii) initially vertical sidewalls take a parabolic shape in the deformed configuration, and (iii) state of stress at any point in the layer is dominated by the hydrostatic pressure. These assumptions result in approximate solutions with reasonable global behaviors such as the effective modulus (Chalhoub and Kelly, 1990, 1991; Koh and Kelly, 1989; Koh and Lim, 2001; Pinarbasi et al., 2006, 2008; Tsai, 2005; Tsai and Lee, 1998) but with less accuracy in stress and displacement fields.

In this paper, full field, closed-form solutions for bonded elastic layers in compression are obtained by separation of variables without any pre-assumption of the stress or displacement. This paper is organized as follows: in Section 2, variable separation of displacement is used to solve the Navier–Cauchy equation of a uniformly compressed axisymmetric solid disk that is perfectly bonded to two parallel rigid plates (Fig. 1(a)). Using similar methods, solutions to annular disks with (Fig. 1(b)) or without (Fig. 1(c)) rigid shaft in the center as well as infinitely long strips (Fig. 1(d)) are obtained and unified in Section 3. In both Sections 2 and 3, finite element modeling (FEM) results are compared with our analytical displacement and stress results. Finally, effective modulus for each case is expressed explicitly and compared with results from FEM as well as other existing analytical and experimental results in Section 4. The layer material in this work is assumed to be isotropic linear elastic and the applied compressive strain ϵ_0 as denoted in Fig. 1 is assumed to be small strain so that nonlinearity is not a consideration in our solutions.

2. Elastic solid disk in compression

2.1. Boundary value problem

A cylindrical coordinate system (r,θ,z) is defined in the right frames of Fig. 1(a). The solid disk with radius a and height h is modeled as linear elastically compressible material with Young's modulus E and Poisson's ratio v which falls into $[-1,0.5)$, with incompressibility to be achieved when v approaches 0.5. The top and bottom surfaces of the solid disk are assumed to be perfectly bonded to two parallel rigid plates, with the bottom plate being fixed. Therefore the uniaxial compressive force P produces a vertical displacement of $-\epsilon_0 h$ for the upper plate.

The Navier–Cauchy equations in cylindrical coordinate system are

$$(1-v)\left(\frac{\partial^2 u_r}{\partial r^2}+\frac{1}{r}\frac{\partial u_r}{\partial r}-\frac{u_r}{r^2}\right)+\frac{1}{2}\frac{\partial^2 u_z}{\partial r\partial z}+\frac{1-2v}{2}\frac{\partial^2 u_r}{\partial z^2}=0 \quad (1)$$

$$(1-v)\frac{\partial^2 u_z}{\partial z^2}+\frac{1}{2}\left(\frac{\partial^2 u_r}{\partial r\partial z}+\frac{1}{r}\frac{\partial u_r}{\partial z}\right)+\frac{1-2v}{2}\left(\frac{\partial^2 u_z}{\partial r^2}+\frac{1}{r}\frac{\partial u_z}{\partial r}\right)=0 \quad (2)$$

where u_r and u_z denote the displacements in radial and axial directions, respectively. Due to the axisymmetry, u_r and u_z are mere

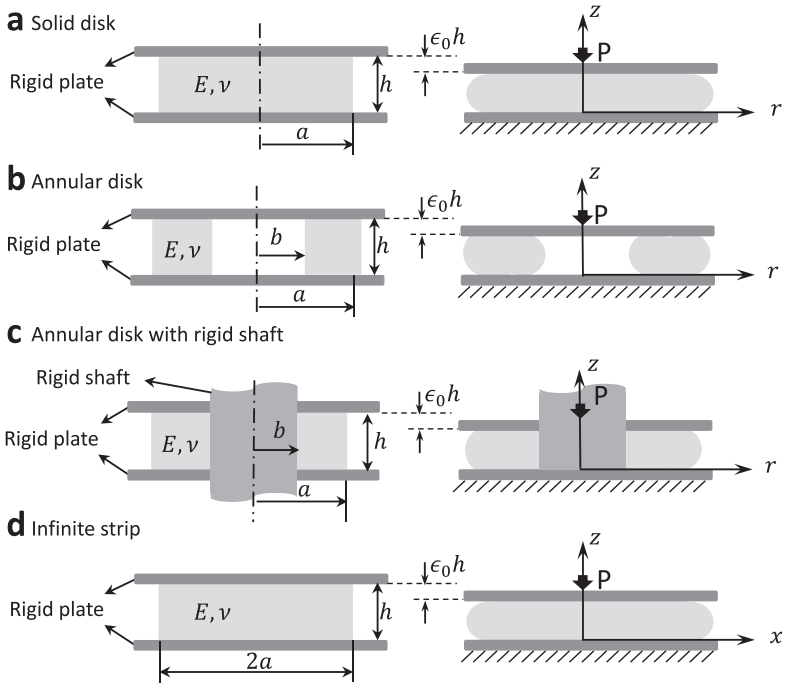

Fig. 1. Cross-sectional views of elastic layers of Young's modulus E, Poisson's ratio, and height h perfectly bonded to parallel rigid plates under uniaxial compressive strain of ϵ_0: (a) axisymmetric solid disk with outer radius a, (b) axisymmetric annular disk with inner radius b, (c) axisymmetric annular disk with rigid shaft in the center, and (d) plane strain model of infinitely long strip with width $2a$.

functions of r and z. Since the solid disk is bonded to a fixed bottom plate and subjected to no tractions on the sidewall, the BCs are given by

$$\begin{aligned} &z=0: \ u_r=u_z=0\\ &z=h: \ u_r=0, \quad u_z=-\epsilon_0 h\\ &r=a: \ \sigma_r=\tau_{rz}=0 \end{aligned} \tag{3}$$

2.2. Analytical solution

To solve the BVP outlined in Section 2.1, instead of assuming the following parabolic budging profile used by Gent and Lindley (1959) and Gent and Meinecke (1970) and many others (Chalhoub and Kelly, 1990; Suh, 2007; Tsai and Lee, 1998):

$$u_r(r,z)=F(r)\left(\frac{z}{h}-\frac{z^2}{h^2}\right) \tag{4}$$

we just assume that $u_r(r,z)$ is variable separable in order to achieve higher accuracy of the displacement field:

$$u_r(r,z)=F(r)G(z) \tag{5}$$

Based on the essential BCs in Eq. (3) and the mirror symmetry with respect to $z=h/2$, the following BCs for $G(z)$ can be obtained:

$$G(0)=G(h)=G'(h/2)=0 \quad \text{and} \quad G'(0)=-G'(h) \tag{6}$$

Plugging Eq. (5) into Eq. (1) and integrating twice with respect to r and z, respectively, u_z is found to be

$$u_z=-2\left[(1-\nu)\left(F'+\frac{F}{r}\right)\Big|_0^r\int_0^z G d\eta+\frac{1-2\nu}{2}G'\Big|_0^z\int_0^r F d\xi\right] + M(z)+N(r) \tag{7}$$

where $M(z)$ and $N(r)$ are to be determined by BCs. According to Eq. (3), $u_z|_{z=0}=0$, we obtain $N(r)=0$ and $M(0)=0$. Also, since $u_z|_{z=h}=-\epsilon_0 h$, terms in $u_z(r,h)$ related with r should be constant, i.e.

$$(1-\nu)\left(F'+\frac{F}{r}\right)\Big|_0^r\int_0^h G d\eta+\frac{1-2\nu}{2}G'\Big|_0^h\int_0^r F d\xi=const \tag{8}$$

The constant on the right hand side has to be zero because the left hand side of Eq. (8) is zero when setting $r=0$. As a result, $M(h)$ can only be $-\epsilon_0 h$ and Eq. (8) becomes

$$\left(F'+\frac{F}{r}\right)\Big|_0^r=\frac{\alpha^2}{h^2}\int_0^r F d\xi \tag{9}$$

where

$$\frac{\alpha^2}{h^2}=\frac{1-2\nu}{1-\nu}\frac{G'(0)}{\int_0^h G d\eta}=\frac{1-2\nu}{1-\nu}\lambda \tag{10}$$

$\lambda=G'(0)/\int_0^h G d\eta$ is assumed to be positive for the current derivation. Zero and negative λ's are discussed in the Appendix A and they are proved to be physically impossible. Taking a derivative on both sides of Eq. (9) gives us

$$F''+\frac{F'}{r}-\frac{F}{r^2}=\frac{\alpha^2}{h^2}F \tag{11}$$

The general solution to the above ordinary differential equation (ODE) is

$$F(r)=C_1 I_1(\alpha r/h)+C_2 K_1(\alpha r/h) \tag{12}$$

where C_1 and C_2 are integration constants and I_i and K_i are the ith order of the modified Bessel function of the first and second kind, respectively. Allowing no void at the center of the solid disk requires $F(0)=0$, which can only be satisfied when $C_2=0$ because of the singularity of $K_1(x)$ at $x=0$. Since C_1 can be absorbed by the $G(z)$ function, F is simplified to be

$$F(r)=I_1(\alpha r/h) \tag{13}$$

Plugging $F(r)$ into Eq. (7), u_z could be rewritten as

$$u_z=-2\left[(1-\nu)\frac{\alpha^2}{h^2}\int_0^z G d\eta+\frac{1-2\nu}{2}G'\Big|_0^z\right]\int_0^r I_1(\alpha\xi/h)d\xi+M(z) \tag{14}$$

with $M(0)=0$ and $M(h)=-\epsilon_0 h$.

So far the displacement field (u_r,u_z) can satisfy Eq. (1) with unknown functions $M(z),G(z)$ as well as the parameter α that need to be determined by Eq. (2). Plugging Eqs. (5) and (14) into Eq. (2), we could obtain two differential equations in order to satisfy Eq. (2) exactly:

$$G'''+2\frac{\alpha^2}{h^2}G'+\frac{\alpha^4}{h^4}\int_0^z G d\eta=\frac{1-2\nu}{2(1-\nu)}\frac{\alpha^2}{h^2}G'(0) \tag{15}$$

and

$$M''+2\left[(1-\nu)\frac{\alpha}{h}G'+\frac{h}{\alpha}\frac{1-2\nu}{2}G'''\right]=0 \tag{16}$$

Eq. (15) is the ODE from which $G(z)$ could be solved and we can then use $G(z)$ to solve $M(z)$ through Eq. (16). The general solution to Eq. (15) is

$$G(z)=(D_1(3-4\nu)/\alpha+D_2 z/h)\sin(\alpha z/h)+(D_3+D_1 z/h)\cos(\alpha z/h) \tag{17}$$

where $D_i(i=1,2,3)$ are integration constants. According to the BCs of $G(z)$ listed in Eq. (6), we can obtain

$$\begin{bmatrix} \frac{3-4\nu}{\alpha}\sin(\alpha)+\cos(\alpha) & \sin(\alpha)\\ 8(1-\nu)\cos(\frac{\alpha}{2})-\alpha\sin(\frac{\alpha}{2}) & \alpha\cos(\frac{\alpha}{2})+2\sin(\frac{\alpha}{2}) \end{bmatrix}\begin{bmatrix} D_1\\ D_2 \end{bmatrix}=0 \tag{18}$$

and $D_3=0$. To ensure that $G(z)$ is a non-trivial function, the determinant of the coefficient matrix in Eq. (18) should be zero, which yields the following characteristic equation:

$$[\alpha\cos(\alpha/2)-2\sin(\alpha/2)][\alpha-(3-4\nu)\sin(\alpha)]=0 \tag{19}$$

Apparently, $\alpha/2=\tan(\alpha/2)$ and $\alpha=(3-4\nu)\sin(\alpha)$ can give us two solutions of the $G(z)$ function. However, the α and $G(z)$ combination must be able to satisfy Eq. (10) and only the function $G(z)$ determined by $\alpha=(3-4\nu)\sin(\alpha)$ can always meet this requirement. Thus, the parameter α is solely dependent on the Poisson's ratio ν and can be obtained by solving

$$\alpha=(3-4\nu)\sin(\alpha) \tag{20}$$

For every allowable Poisson's ratio, $\nu\in[-1,0.5)$, there is one and only one nonzero solution for α. The corresponding $G(z)$ will take the following expression

$$G(z)=A_1 G_+(z) \tag{21}$$

where A_1 is a constant with the unit of length and

$$G_\pm=[\sin(\alpha z/h)(1-z/h)\pm\sin(\alpha(1-z/h))(z/h)] \tag{22}$$

Note that as $\nu\to0.5,\alpha\to0$ and Eq. (22) turns to

$$G_+\to 2\alpha\left(\frac{z}{h}-\frac{z^2}{h^2}\right) \tag{23}$$

which is the very popular but empirical parabolic bulging assumption as mentioned in Eq. (4) and we now find a theoretical origin for it.

Using Eq. (21) and the BCs $M(0)=0,M(h)=-\epsilon_0 h$, M is solved from Eq. (16) as

$$M=A_1\cot(\alpha/2)G_- -\epsilon_0 z \tag{24}$$

where G_- is given by Eq. (22).

With the solutions of $F(r)$ given by Eq. (12), $G(z)$ given by Eq. (21), and $M(z)$ given by Eq. (24), the displacement field for the elastically compressible disk is finally solved as

$$\begin{aligned} u_r^S &= A_1 G_+ I_1(\alpha r/h) \\ u_z^S &= A_1 \cot(\alpha/2) G_- I_0(\alpha r/h) - \epsilon_0 z \end{aligned} \tag{25}$$

where the superscript S indicates results for solid disks and the constant A_1 is the only left unknown which will be determined through the weak form of the traction-free BC at $r = a$, i.e. $\langle \sigma_r \rangle|_{r=a} = \langle \tau_{rz} \rangle|_{r=a} = \langle \tau_{r\theta} \rangle|_{r=a} = 0$, where $\langle \cdot \rangle$ is defined as $\langle \cdot \rangle = \int_0^h \cdot \, dz/h$. And it is found that $\langle \tau_{rz} \rangle|_{r=a} = 0$ and $\langle \tau_{r\theta} \rangle|_{r=a} = 0$ are automatically satisfied once $G_\pm(z)$ is obtained, such that A_1 is solely determine by

$$\langle \sigma_r \rangle|_{r=a} = 0 \tag{26}$$

Thus, based on linear elastic constitutive law and small strain kinematics, A_1 can be solved as

$$A_1 = \frac{\nu(3-4\nu)\epsilon_0 h}{4(1-2\nu)Q_1} \tag{27}$$

where $Q_1 = [I_0(\omega) + (1-2\nu)I_2(\omega)]/2$ and $\omega = \alpha a/h$.

With analytical solutions of the displacement field, the stress field can be derived through kinematics and constitutive laws based on linear elasticity and are shown as:

$$\begin{aligned} \sigma_r^S &= \frac{\nu E \epsilon_0}{(1+\nu)(1-2\nu)} \left[\frac{\alpha\nu}{2Q_1} \cot\left(\frac{\alpha}{2}\right) I_0\left(\frac{\alpha r}{h}\right) g_1(z) - \frac{3-4\nu}{4Q_1} I_1\left(\frac{\alpha r}{h}\right) \frac{h}{r} G_+ - 1 \right] \\ \sigma_\theta^S &= \frac{\nu E \epsilon_0}{(1+\nu)(1-2\nu)} \left[\frac{\alpha\nu}{2Q_1} \cot\left(\frac{\alpha}{2}\right) I_0\left(\frac{\alpha r}{h}\right) g_2(z) + \frac{3-4\nu}{4Q_1} I_1\left(\frac{\alpha r}{h}\right) \frac{h}{r} G_+ - 1 \right] \\ \sigma_z^S &= \frac{(1-\nu) E \epsilon_0}{(1+\nu)(1-2\nu)} \left[\frac{\alpha\nu}{2Q_1} \cot\left(\frac{\alpha}{2}\right) I_0\left(\frac{\alpha r}{h}\right) g_3(z) - 1 \right] \\ \tau_{rz}^S &= \frac{\alpha\nu(1-\nu) E \epsilon_0}{2(1+\nu)(1-2\nu)Q_1} I_1(\alpha r/h) g_4(z) \end{aligned} \tag{28}$$

where

$$\begin{aligned} g_1(z) &= \frac{\alpha p_1(z) - 3q_1(z)/2}{\cos(\alpha/2)(\alpha - 3\sin(\alpha))} \\ g_2(z) &= \cos\left(\left(\tfrac{1}{2} - \tfrac{z}{h}\right)\alpha\right) / \cos\left(\tfrac{\alpha}{2}\right) \\ g_3(z) &= \frac{\alpha p_1(z) + q_1(z)/2}{\cos(\alpha/2)(\alpha + \sin(\alpha))} \\ g_4(z) &= -\frac{\alpha p_2(z) + q_2(z)/2}{\sin(\alpha/2)(\alpha + \sin(\alpha))} \end{aligned} \tag{29}$$

and

$$\begin{aligned} p_1(z) &= \tfrac{z}{h} \cos\left(\left(\tfrac{3}{2} - \tfrac{z}{h}\right)\alpha\right) + \left(1 - \tfrac{z}{h}\right) \cos\left(\left(\tfrac{1}{2} + \tfrac{z}{h}\right)\alpha\right) \\ q_1(z) &= \sin\left(\left(\tfrac{3}{2} - \tfrac{z}{h}\right)\alpha\right) + \sin\left(\left(\tfrac{1}{2} + \tfrac{z}{h}\right)\alpha\right) \\ p_2(z) &= \tfrac{z}{h} \sin\left(\left(\tfrac{3}{2} - \tfrac{z}{h}\right)\alpha\right) - \left(1 - \tfrac{z}{h}\right) \sin\left(\left(\tfrac{1}{2} + \tfrac{z}{h}\right)\alpha\right) \\ q_2(z) &= \cos\left(\left(\tfrac{3}{2} - \tfrac{z}{h}\right)\alpha\right) - \cos\left(\left(\tfrac{1}{2} + \tfrac{z}{h}\right)\alpha\right) \end{aligned} \tag{30}$$

2.3. Numerical results

To validate our analytical solutions, we have conducted FEM using commercial software ABAQUS v6.10. An axisymmetric solid disk with Young's modulus of 50 MPa is modeled with CAX4IH elements under uniaxial compressive strain $\epsilon_0 = 5\%$ between parallel rigid plates using the BCs depicted in Fig. 1(a) and outlined in Eq. (3). A full field comparison between FEM results (left column) and analytical results (right column) with exactly the same color scale is shown in Fig. 2. Except the edges ($r = a$) where only the weak form of the natural BCs is satisfied, analytical and FEM results of both displacement and stress fields have demonstrated remarkable full field agreement. Thus compared to existing analytical solutions of elastic disks in compression, our full field analytical solution is competitive in terms of both simplicity and accuracy.

Graphical comparison between analytical and FEM results of displacement and stress are offered in Figs. 3 and 4, respectively. Fig. 3(a) shows the normalized lateral displacement $u_r/\epsilon_0 h$ as a function of z at $r = a$, i.e. the bulging profile at the sidewall of the disk, for various Poisson's ratios (ν = 0.3, 0.45, 0.49 and 0.5) with fixed aspect ratio ($a/h = 5$). The good agreement between analytical and FEM results over a wide range of Poisson's ratio indicates that we have found a generic and accurate analytical solution for elastically compressible solid disks. When ν = 0.5, the analytical and FEM results are also compared with the parabolic displacement which is widely assumed for incompressible disks in the pressure method. It is evident in Fig. 3(a) and Eq. (23) that our solution can successfully degenerate to the parabolic bulging shape. Note that a much flatter bulging profile was observed in Mott and Roland's compression experiments (Mott and Roland, 1995) on bonded slender rubber cylinders ($0.22 < a/h < 0.54$). Later on, without pre-assuming the lateral bulging shape, Horton, Tupholme and Gover obtained nonparabolic bulging profiles (Horton et al., 2002; Horton et al., 2003) for bonded rubber blocks under axially loading, which qualitatively captured this flatter profile for small aspect ratio in Mott and Roland's experiments (Mott and Roland, 1995) and can decay to parabola-like shape when the aspect ratio is large (e.g. $a/h > 1$). The bulging profile given by Eq. (25) is always parabola-like for allowable Poisson's ratio such that it more successfully captures the displacement of bonded blocks with large aspect ratios (e.g. $a/h > 1$).

At the aspect ratio of $a/h = 5$, the maximum lateral bulging displacement of incompressible layers can be almost four times of the

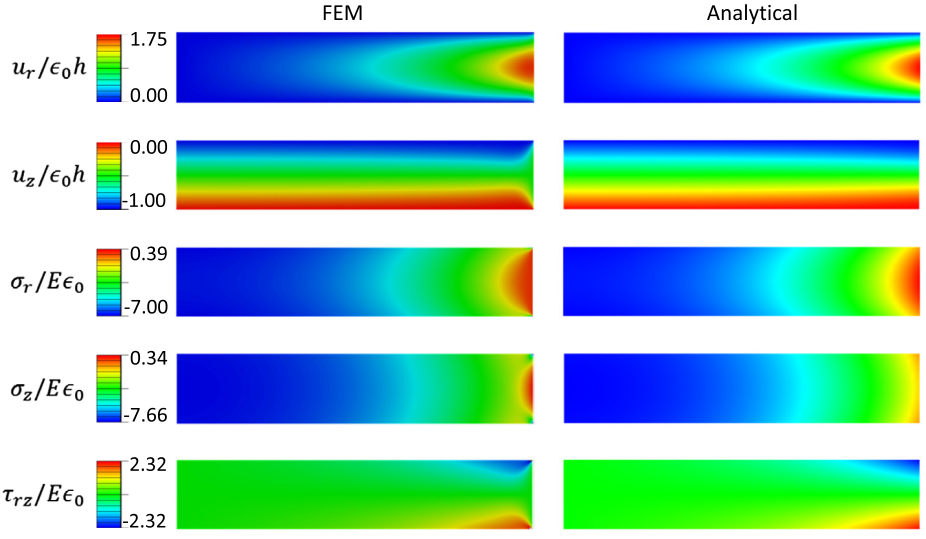

Fig. 2. Contour plots of both FEM (left column) and analytical (right column) results of displacement and stress fields of a solid disk in compression. Analytical displacements are given by Eq. (25) and stresses are given by Eq. (28). Parameters used in this example are: $a/h = 5$, $\nu = 0.48$ and $\epsilon_0 = 5\%$.

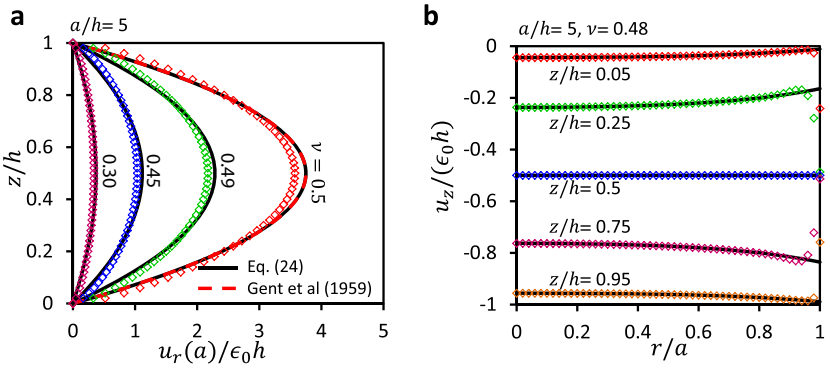

Fig. 3. Comparison between analytical and FEM results of displacements (a) u_r and (b) u_z of solid disks in compression. Solid curves represent analytical solutions as given by Eq. (25), which is compared with Gent's solution for incompressible material (Gent and Lindley, 1959). Markers represent FEM results.

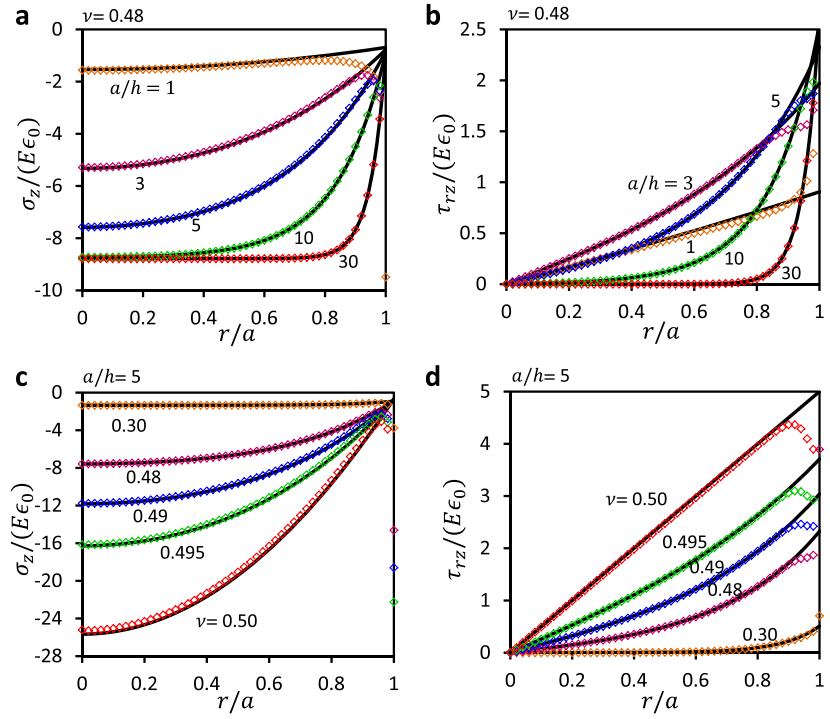

Fig. 4. Comparison between analytical and FEM results of interfacial stresses of solid circular disks with (a) and (b) fixed Poisson's ratio and (c) and (d) fixed aspect ratio. Solid curves represent analytical solutions given by Eq. (31) and markers represent FEM results.

applied axial compressive displacement, $\epsilon_0 h$, and almost ten times larger compared to layers with $\nu = 0.3$. Fig. 3(b) exhibits the distribution of vertical displacement $u_z/\epsilon_0 h$ along the radial direction at fixed aspect ratio and Poisson's ratio ($a/h = 5, \nu = 0.48$) at different vertical positions (z/h = 0.05, 0.25, 0.5, 0.75 and 0.95). It is evident that our analytical results can closely match with FEM results except a small region around the edge where $r/a = 1$, which is due to the weak form of the traction free BC we have adopted in Eq. (26). Such discrepancy at the edge has shown up in the full field comparison in Fig. 2 and will also appear in the later comparison of stress distribution. According to both FEM and theoretical results, it is clear that unlike one of the basic assumptions adopted by the pressure method that all horizontal planes remain planar, only the top (z/h = 1), middle (z/h = 0.5), and bottom (z/h = 0) horizontal planes (z/h = 0.5) remain perfect planar after deformation whereas other horizontal planes remain planar when close to the axial center but start to bend toward the edge.

Graphical comparison of analytical vs. FEM stresses are offered at the elastic layer-rigid plate interface. By setting $z = 0$ in Eq. (28), we can get:

$$\begin{aligned}
\sigma_r^S &= \sigma_\theta^S = \frac{\nu E\epsilon_0}{(1+\nu)(1-2\nu)}\left[\frac{\alpha\nu}{2Q_1}\cot\left(\frac{\alpha}{2}\right)I_0\left(\frac{\alpha r}{h}\right) - 1\right] \\
\sigma_z^S &= \frac{(1-\nu)E\epsilon_0}{(1+\nu)(1-2\nu)}\left[\frac{\alpha\nu}{2Q_1}\cot\left(\frac{\alpha}{2}\right)I_0\left(\frac{\alpha r}{h}\right) - 1\right] \\
\tau_{rz}^S &= \frac{\alpha\nu(1-\nu)E\epsilon_0}{2(1+\nu)(1-2\nu)Q_1}I_1(\alpha r/h)
\end{aligned} \tag{31}$$

for $0 \leqslant r \leqslant a$. The analytical and FEM results are plot in Fig. 4 for various aspect ratios and Poisson's ratios and our FEM results show negligible difference compared to the numerical results in (Yeoh et al., 2002) performed by ANSYS. Still, due to the discontinuous BCs and the non-uniform deformation around the edges ($z = 0, h$ and $r = a$), stress concentrations are expected and were observed both numerically (Imbimbo and De Luca, 1998; Suh, 2007; Yeoh et al., 2002) and experimentally (Gent et al., 1974; Sakai, 1995). Although stress singularities are not captured by Eqs. (28) and (31), conclusions could still be drawn from Fig. 4.

A feature common to all layers is that normal stress decays from center to edge whereas shear stress builds up towards the edge. Fig. 4(a) and (b) focus on fixed Poisson's ratio (ν = 0.48) with different aspect ratios (a/h = 1, 3, 5, 10 and 30). According to Fig. 4(a),

with all other conditions the same, disks with larger aspect ratio will experience higher pressure on the surfaces. According to Fig. 4(b), the shear stress is large when the aspect ratio is small in general whereas abnormal behavior has been found for $a/h = 1$ due to the edge effects. Fig. 4(c) and (d) focus on fixed aspect ratio ($a/h = 5$) with different Poisson's ratios ($\nu = 0.3$, 0.48, 0.49, 0.495 and 0.5). According to Fig. 4(c), with all other conditions the same, disks with larger Poisson's ratio will experience higher pressure on the surfaces. According to Fig. 4(d), the shear stress linearly increases with the radial coordinate for incompressible disks, as will be discussed in Section 4.2. The shear stress diminishes with Poisson's ratio and when $\nu = 0.3$, the shear stress almost vanishes completely, which echoes with the small bulging displacements as shown in Fig. 3(a).

3. Solutions for other configurations

The analytical method established for solid disks in Section 2 can be extended to obtain solutions for elastic layers of other configurations. For example, annular disks are widely used as gasket, seal and seismic isolation structures, which are often under uniaxial compression between two rigid plates just as shown in Fig. 1(b). Sometimes there might even be a rigid shaft going through the circular hole of the annular disk, as shown in Fig. 1(c). Another example is rectangular elastomer stamps used in transfer-printing, which can be approximated as infinitely long strips as shown in Fig. 1(d). Note that 3D rectangular PDMS stamps are more commonly used in lab scale transfer-printing of nanomaterials and applying our method to bonded 3D rectangular layers under compression (Koh and Lim, 2001; Tsai, 2005) is left as a future work. In this section we will briefly discuss the analytical solutions for these three configurations (Fig. 1(b)–(d)) using the same methods developed in Section 2.

3.1. Boundary conditions

For annular disks in compression shown in Fig. 1(b), all of the essential BCs given by Eq. (3) still hold and therefore Eqs. (7)–(12) are still applicable. The only difference before applying natural BCs is that $F(0) = 0$ is no longer true. Therefor u_r has to take the following form

$$u_r = G_+[A_2 I_1(\alpha r/h) + A_3 K_1(\alpha r/h)] \tag{32}$$

which is similar to the expression obtained by Tsai (2012) but with different construction of G_+. As u_r is assumed to be parabolically dependent on z in Tsai (2012) but we do not have to make this assumption, the coefficient α in our paper is different from that in Tsai (2012). A_2 and A_3 are to be determined by the weak form of traction-free conditions at both $r = a$ and $r = b$, where a and b are the outer and inner radii of the annular disk, i.e.

$$\langle \sigma_r \rangle|_{r=a} = \langle \sigma_r \rangle|_{r=b} = 0 \tag{33}$$

When there is a rigid frictionless shaft co-axially aligned within the annular disk, as shown in Fig. 1(c), the outer wall remains traction free while the BC for the inner wall becomes

$$u_r(b,z) = 0, \quad \tau_{rz}(b,z) = 0 \tag{34}$$

The infinitely long strip is assumed to be under plane strain condition as shown in Fig. 1(d). The corresponding natural BC is traction free at the edges:

$$\langle \sigma_x \rangle|_{x=\pm a} = 0 \tag{35}$$

3.2. Displacement solutions

Following the similar process developed in Section 2, and applying BCs given by Eqs. (33)–(35), the displacement solutions for the different configurations are obtained as follows with $G_\pm$ given by Eq. (22): solid disks:

$$\begin{aligned} u_r^S(r,z) &= A_1 G_+ I_1(\alpha r/h) \\ u_z^S(r,z) &= A_1 \cot(\alpha/2) G_- I_0(\alpha r/h) - \epsilon_0 z \end{aligned} \tag{36}$$

annular disks:

$$\begin{aligned} u_r^A(r,z) &= G_+[A_2 I_1(\alpha r/h) + A_3 K_1(\alpha r/h)] \\ u_z^A(r,z) &= \cot(\alpha/2) G_-[A_2 I_0(\alpha r/h) - A_3 K_0(\alpha r/h)] - \epsilon_0 z \end{aligned} \tag{37}$$

annular disks with rigid shaft:

$$\begin{aligned} u_r^{AR}(r,z) &= A_4 G_+[I_1(\alpha r/h) - \Lambda K_1(\alpha r/h)] \\ u_z^{AR}(r,z) &= A_4 \cot(\alpha/2) G_-[I_0(\alpha r/h) + \Lambda K_0(\alpha r/h)] - \epsilon_0 z \end{aligned} \tag{38}$$

infinitely long strips:

$$\begin{aligned} u_x^I(x,z) &= A_5 G_+ \mathrm{sh}(\alpha x/h) \\ u_z^I(x,z) &= A_5 \cot(\alpha/2) G_- \mathrm{ch}(\alpha x/h) - \epsilon_0 z \end{aligned} \tag{39}$$

where

$$A_i = \frac{\nu(3-4\nu)\epsilon_0 h}{4(1-2\nu)Q_i}, \quad i = 1,2,3,4,5 \tag{40}$$

where

$$\begin{aligned} Q_1 &= [I_0(\omega) + (1-2\nu) I_2(\omega)]/2 \\ Q_2 &= D/(Q_{22} - Q_{12}) \\ Q_3 &= D/(Q_{11} - Q_{21}) \\ Q_4 &= (1-\nu)[I_0(\omega) + \Lambda K_0(\omega)] - (1-2\nu)[I_1(\omega) - \Lambda K_1(\omega)]/\omega \\ Q_5 &= (1-\nu) ch(\omega) \end{aligned} \tag{41}$$

$$D = \det\left(\begin{bmatrix} Q_{11} & Q_{12} \\ Q_{21} & Q_{22} \end{bmatrix}\right) \tag{42}$$

$$\begin{aligned} Q_{11} &= \tfrac{1}{2}[I_0(\omega) + (1-2\nu) I_2(\omega)], \quad Q_{12} = -\tfrac{1}{2}[K_0(\omega) + (1-2\nu) K_2(\omega)] \\ Q_{21} &= \tfrac{1}{2}[I_0(\varsigma) + (1-2\nu) I_2(\varsigma)], \quad Q_{22} = -\tfrac{1}{2}[K_0(\varsigma) + (1-2\nu) K_2(\varsigma)] \end{aligned} \tag{43}$$

where $\omega = \alpha a/h$, $\varsigma = \alpha b/h$ and $\Lambda = I_1(\varsigma)/K_1(\varsigma)$. Note that Q_1 and Q_5 are dependent on the Poisson's ratio ν and the aspect ratio a/h, while Q_2, Q_3 and Q_4 also depend on the radius ratio b/a. The superscript in each formula is used to denote the shape of the elastic layer: S for solid disks, A for annular disks, AR for annular disks with rigid shafts and I for infinitely long strips. These solutions can exactly satisfy the equilibrium equations as well as all the essential BCs, while weakly satisfy the natural BCs.

The comparisons between analytical and FEM displacements for annular disks, annular disks with rigid shafts and infinitely long strips are shown in Fig. 5–7, respectively. Similar to Fig. 3, our analytical solutions for annular disks can successfully capture the displacement with high precision when $a/h > 1$. Fig. 5(a) indicates that for annular disks, the maximum bulge displacement at the inner wall may exceed that at the outer wall, depending on the b/a ratio. For materials close to incompressible, a comparison between Figs. 3(a), 5(a), 6(a) and 7(a) suggests that the maximum lateral bulging displacement of the outer sidewall will increase in the following order: annular disk, annular disk with rigid shaft, solid disk and infinitely long strip. Annular disk exhibits the smallest budging displacement because it can extrude both inward and outward. Although annular disk with rigid shaft cannot extrude inward, it contains less materials compared to solid disks. Since infinitely long strip simplified to plane strain model does not allow strain in y direction, the largest budging displacement is observed in the infinitely long strip among the four configurations we have

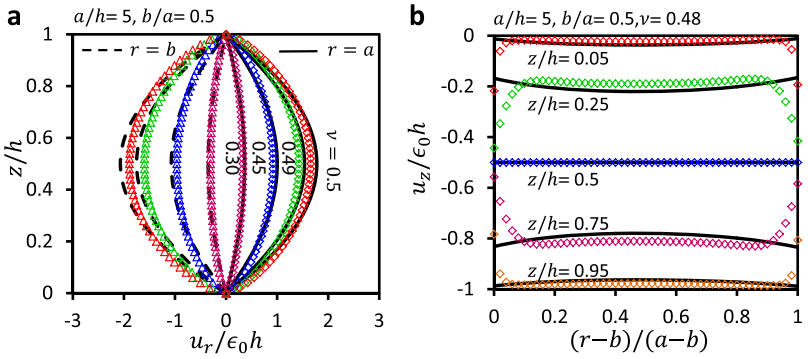

Fig. 5. Comparison between analytical and FEM results of displacements (a) u_r and (b) u_z of annular disks as depicted in Fig. 1(b). Solid curves represent analytical solutions given by Eq. (37) and markers represent FEM results.

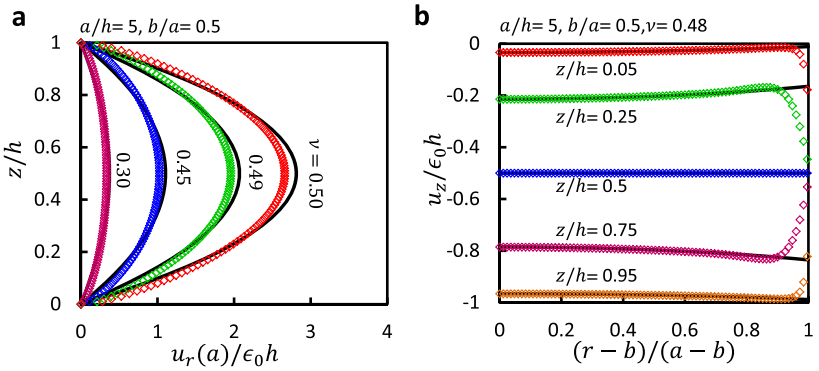

Fig. 6. Comparison between analytical and FEM results of displacements (a) u_r and (b) u_z of annular disks with rigid shafts as depicted in Fig. 1(c). Solid curves represent analytical solutions given by Eq. (38) and markers represent FEM results.

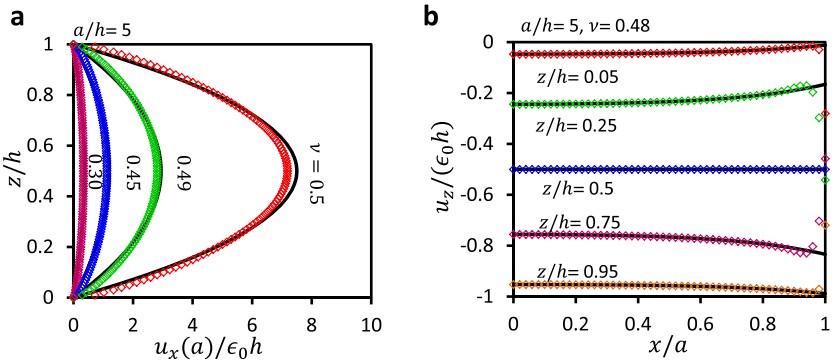

Fig. 7. Comparison between analytical and FEM results of displacements (a) u_r and (b) u_z of infinitely long strips as depicted in Fig. 1(d). Solid curves represent analytical solutions given by Eq. (39) and markers represent FEM results.

solved. Because of the same reasons, the effect of Poisson's ratio on the budging displacements is the least in annular disks while the most significant in infinitely long strips. Vertical displacements as shown in Figs. 5(b), 6(b) and 7(b) share a lot of similarity with the solid disks as shown in Fig. 3(a): only planes well inside the material remain planar whereas planes far from the middle plane ($z = h/2$) and the symmetric axis always bend.

3.3. Interfacial stresses

After obtaining the displacement fields of different configurations of elastic layers in Section 3.2, the full stress fields can be derived though kinematics and constitutive relations, similar to Eq. (27). When setting $z = 0$, interfacial stress components for various configurations are given by the following unified expression:

$$\sigma_1 = \sigma_2 = \frac{\nu}{1-\nu}\sigma_3 = \frac{\nu E\epsilon_0}{(1+\nu)(1-2\nu)}\left[\frac{\alpha\nu}{2}\cot\left(\frac{\alpha}{2}\right)\Phi - 1\right]$$
$$\tau = \frac{\alpha\nu(1-\nu)E\epsilon_0}{2(1+\nu)(1-2\nu)}\Psi \tag{44}$$

where Φ and Ψ are two shape-related functions and are expressed as follows: solid disks ($0 \leqslant r \leqslant a$):

$$\Phi = I_0(\alpha r/h)/Q_1, \quad \Psi = I_1(\alpha r/h)/Q_1 \tag{45}$$

annular disks ($b \leqslant r \leqslant a$):

$$\Phi = I_0(\alpha r/h)/Q_2 - K_0(\alpha r/h)/Q_3, \quad \Psi = I_1(\alpha r/h)/Q_2 + K_1(\alpha r/h)/Q_3 \tag{46}$$

annular disks with rigid shaft ($b \leqslant r \leqslant a$):

$$\Phi = [I_0(\alpha r/h) + \Lambda K_0(\alpha r/h)]/Q_4, \quad \Psi = [I_1(\alpha r/h) - \Lambda K_1(\alpha r/h)]/Q_4 \tag{47}$$

and infinitely long strips ($-a \leqslant x \leqslant a$):

$$\Phi = ch(\alpha x/h)/Q_5, \quad \Psi = sh(\alpha x/h)/Q_5 \tag{48}$$

where $\sigma_1 = \sigma_r, \sigma_2 = \sigma_\theta, \sigma_3 = \sigma_z, \tau = \tau_{rz}$ for cylindrical coordinates and $\sigma_1 = \sigma_x, \sigma_2 = \sigma_y, \sigma_3 = \sigma_z, \tau = \tau_{xz}$ for rectangular coordinates, and Q_i are given in Eq. (40). When $b \to 0$, the solution for annular disks (Eq. (46)) or annular disks with rigid shaft (Eq. (47)) will decay to solid disks (Eq. (45)), which indicates that solid disk is the special case of annular disks when the inner radius is zero.

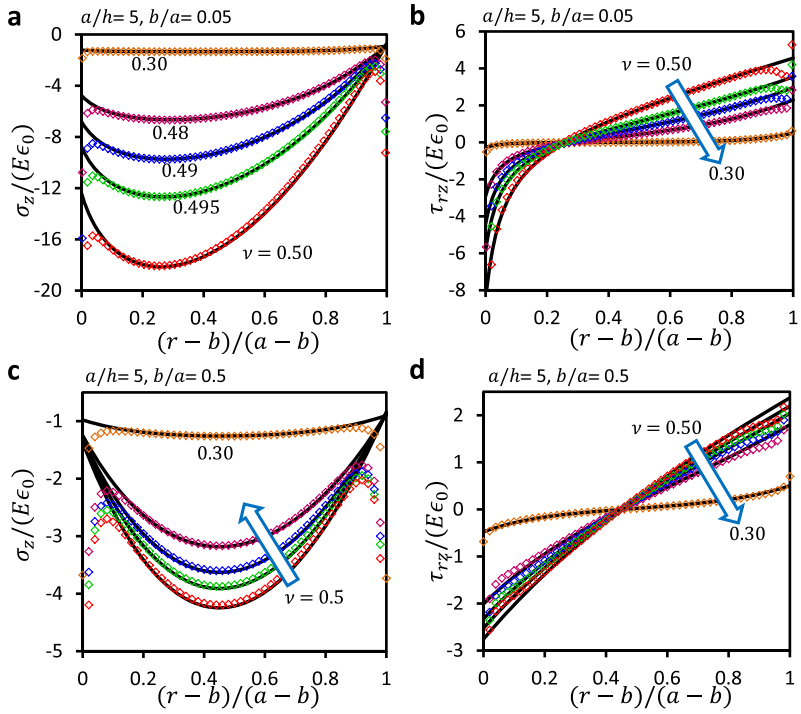

Fig. 8. Comparison between analytical and FEM stresses of annular disks with constant aspect ratio ($a/h = 5$) and different radius ratios: $b/a = 0.05$ for (a) and (c); $b/a = 0.5$ for (b) and (d).

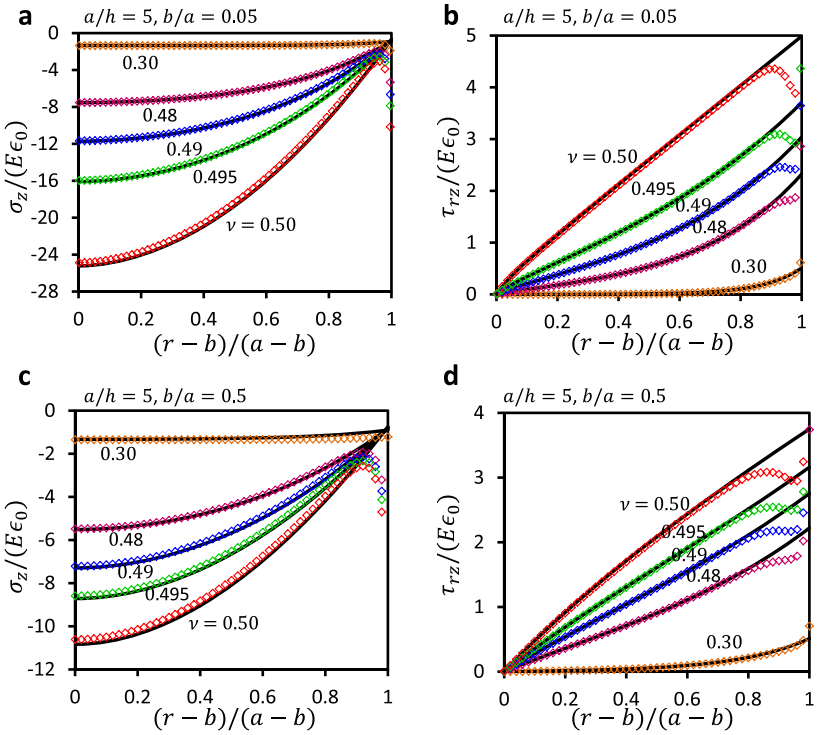

Fig. 9. Comparison between analytical and FEM stresses of annular disks with rigid shafts with constant aspect ratio ($a/h = 5$) and different radius ratios: $b/a = 0.05$ for (a) and (c); $b/a = 0.5$ for (b) and (d).

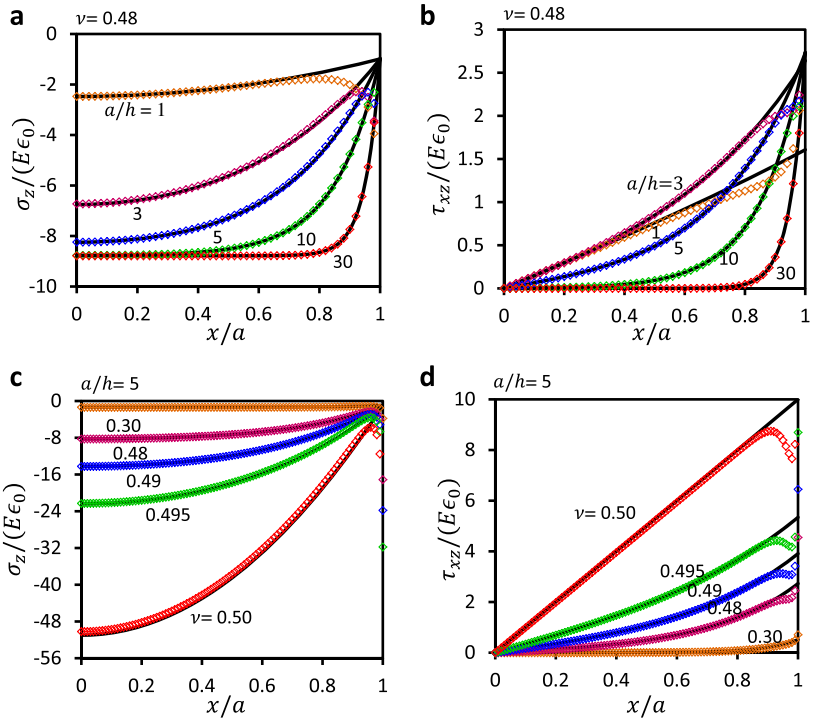

Fig. 10. Comparison between analytical and FEM stresses of infinite strips: (a) and (b) fixed Poisson's ratio (0.48) but different aspect ratios; (c) and (d) fixed aspect ratio ($a/h = 5$) but different Poisson's ratios.

The comparison between analytical (Eq. (44)) and FEM interfacial stresses is shown in Figs. 8–10 for annular disks, annular disks with rigid shafts, and infinitely long strips, respectively. Together with Fig. 4 of solid disks, we will compare the interfacial stresses in all four configurations. For all cases, the maximum normal stresses always occur far from the traction-free edges whereas the maximum shear stresses are always found at the traction-free edges. Strong dependence of the maximum normal and shear stresses on Poisson's ratio is also evident in the four figures. According to Figs. 4(c) and (d), 8, 9 and 10(c) and (d), layers with larger Poisson's ratios always experience higher normal and shear stresses. When $\nu = 0.3$, the normal and shear stresses are both within a fraction of $E\epsilon_0$ whereas when $\nu = 0.5$, the maximum values of normal and shear stresses are both several times of $E\epsilon_0$. Comparing Figs. 8 and 9, due to the constraints of the rigid shaft, the normal and shear stresses in the annular disks with rigid shafts are slightly higher than those without rigid shafts. Comparing Figs. 8(a) and (b) and 9(a) and (b) with Figs. 8(c) and (d) and 9(c) and (d), it is evident that annular disks with smaller inner radius have to experience larger normal and shear stresses. When $b \to 0$, Figs. 8 and 9 will become exactly like Fig. 4(c) and (d) because the results for annular disks, either with or without the rigid shaft, will fully degenerate to the results for solid disks. Fig. 10 also looks alike Fig. 4 in shapes but the values in Fig. 10 are much higher due to the stronger constraint in the plane strain condition compared to the axisymmetric condition.

4. Discussions

Full field, closed-form displacement and stress solutions for elastically compressible layers of various configurations have been obtained in Section 3. Although we have only worked on compressive loading, the sign of our results can be simply reversed to become the solutions for tensile loading due to the symmetry of this linear elastic BVP. With those results, in this section we want to discuss first, the effective modulus, and second, the degeneration of the solutions of compressible layers to incompressible layers.

4.1. Effective modulus

As mentioned in the beginning of the paper, when elastic layers are subjected to uniaxial compression by perfectly bonded rigid plates, the effective modulus, E_c, defined as the slope of the engineering stress–strain curve can be very different from the Young's modulus of the layer material. For isotropic linear elastic material, the effective modulus can be written as:

$$E_c \equiv \int |\sigma_z| dA_0/(A_0\epsilon_0) \tag{49}$$

where A_0 is the cross-sectional area perpendicular to z direction. However, the areal integrals of our σ_z are slightly dependent on z due to the weakly satisfied natural BCs. To eliminate the z-dependence of the effective modulus, we propose an averaged form of E_c:

$$E_c = \int_0^z \int |\sigma_z| dA_0 dz/(A_0\epsilon_0 h) \tag{50}$$

Based on this definition, normalized effective moduli for the four different configurations are obtained respectively:

$$E_c/E = \frac{(1-\nu)}{(1+\nu)(1-2\nu)}\left[1 - \frac{2\nu^2}{1-\nu}\Gamma\right] \tag{51}$$

where Γ is a shape-related function given as follows: solid disks:

$$\Gamma = \frac{I_1(\omega)}{Q_1\omega} \tag{52}$$

annular disks:

$$\Gamma = \frac{O(\omega) - O(\varsigma)}{(\omega^2 - \varsigma^2)} \text{ with } O(x) = x[I_1(x)/Q_2 + K_1(x)/Q_3] \tag{53}$$

annular disks with rigid shaft:

$$\Gamma = \frac{\omega H}{(\omega^2 - \varsigma^2)Q_4} \text{ with } H = I_1(\omega) - \Lambda K_1(\omega) \tag{54}$$

and infinitely long strips:

$$\Gamma = \frac{\mathrm{sh}(\omega)}{2\omega Q_5} \tag{55}$$

where ω, ς and Q_i's are defined as before.

It is evident from Eqs. (52)–(55) that the normalized effective modulus only depends on the aspect ratio, the radius ratio for annular disks, and the Poisson's ratio of the layer. The comparison between analytical and FEM results are shown in Fig. 11.

The left and right frames of Fig. 11(a) present two different ways to plot Eq. (51) with Γ given by Eq. (52) for the solid disks. In the left frame of Fig. 11(a), the normalized effective modulus is plotted as a function of the aspect ratio for different Poisson's ratios. The effective modulus can drop several folds even when the Poisson's ratio is reduced slightly from 0.5 to 0.4995, indicating ultra-sensitive dependence of effective modulus on the Poisson's ratio of the elastic disks. Effective modulus also decreases with decreased aspect ratio and it approaches 1 when the elastic layer

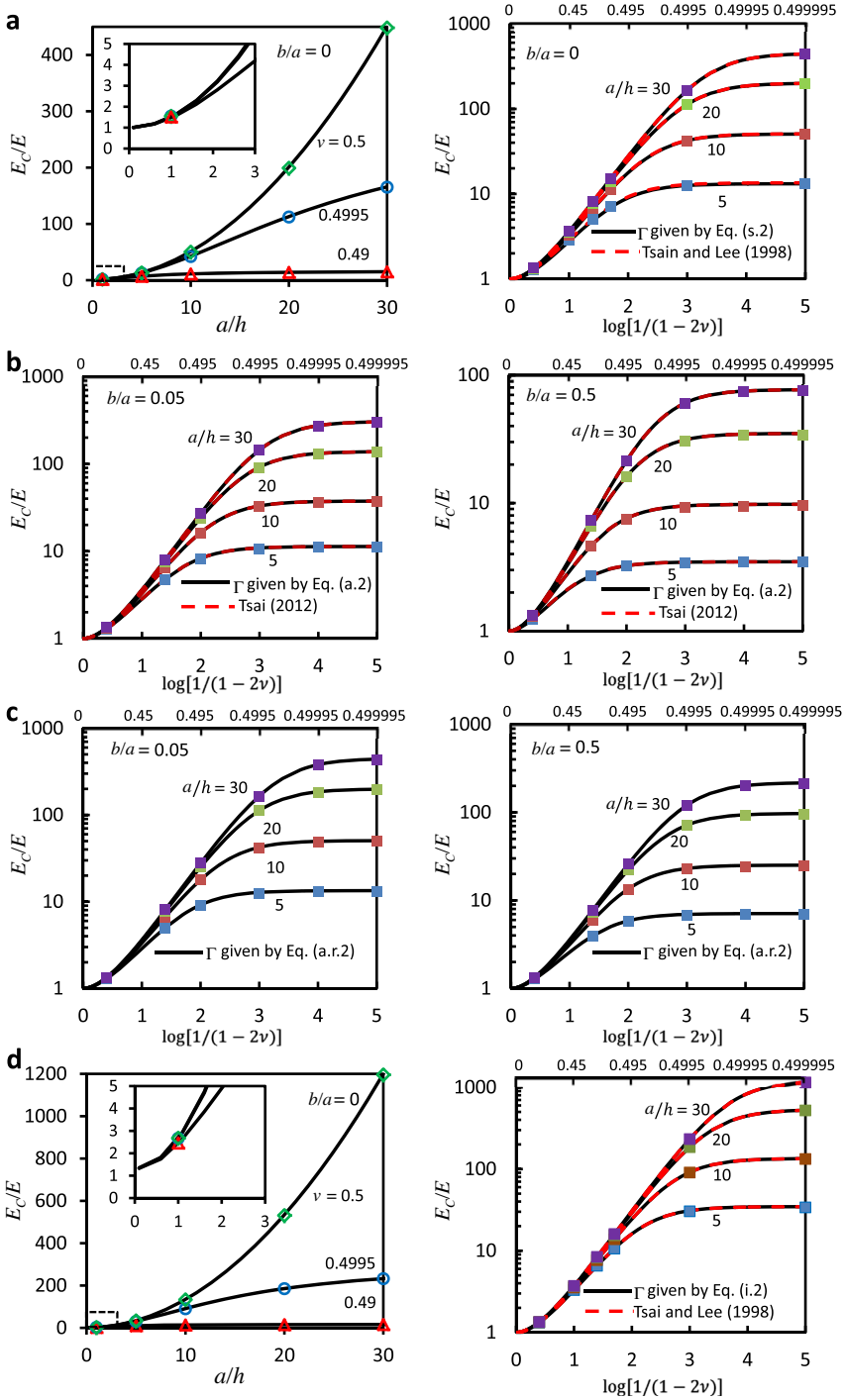

Fig. 11. Comparison between analytical and FEM results of normalized effective moduli of (a) solid disks, (b) annular disks and (c) annular disks with rigid shaft and (d) infinite strips. Results given by Eq. (51) are plotted in black curves and Tsai's results are plotted in dashed red curves whereas FEM results are given by markers. (For interpretation of the references to colour in this figure legend, the reader is referred to the web version of this article.)

becomes a slim bar, i.e. when a/h approaches 0, as shown in the blown-up inset of Fig. 11(a) left frame. Practically uniaxial tension instead of compression tests are usually carried out to test the Young's modulus of a slender sample to avoid buckling instability. The right frame of Fig. 11(a) plots the normalized effective modulus as a function of the Poisson's ratio for different aspect ratios. Instead of using ν as the horizontal axis, we follow the convention in (Tsai and Lee, 1998) and use $\log[1/(1-2\nu)]$ to illustrate the strong sensitivity on ν. Our analytical solution has found perfect consistency with FEM results as well as the analytical solution obtained by the pressure method (Tsai, 2012; Tsai and Lee, 1998) which are plotted in red dashed curves. In (Tsai, 2012; Tsai and Lee, 1998), instead of seeking full field solutions of displacement and stress, authors developed solutions of mean pressure to calculate E_c. The right frame of Fig. 11(a) indicates that when Poisson's ratio approaches 0, i.e. no lateral bulging is expected, effective modulus is strictly Young's modulus whereas effective modulus can increase by more than two orders of magnitude when Poisson's ratio approaches 0.5. Moreover, disks with larger aspect ratios are even more sensitive to Poisson's ratio. It has also been noticed that the analytical models tend to overestimate the effective modulus when the shape factor, $s = a/(2h)$ for solid disks, is large (e.g. >30) compared with experimental measurements (Anderson et al., 2004; Suh, 2007) and the cause is still unclear.

Fig. 11(b) is plotting Eq. (51) with Γ given by Eq. (53) (traction-free annular disks) which are compared with results from Tsai (Tsai, 2012) with two different radius ratios: $b/a = 0.05$ and $b/a = 0.5$, in the left and right frames, respectively. For annular disks with the same outer radius and Poisson's ratio, the ones with smaller inner radius exhibit higher effective modulus. The same conclusion applies to annular disks with rigid shafts as shown in Fig. 11(c). Comparing Fig. 11(b) and (c), everything else the same, annular disks with rigid shafts are stiffer, due to the stronger constraints. Effective moduli for infinitely long strips are plotted in Fig. 11(d) in a format similar to the solid disks as shown in Fig. 11(a). Despite of the similar shapes, effective moduli of infinitely long strips are slightly greater than those of solid disks.

The known dependence of effective modulus on Young's modulus, Poisson's ratio, and aspect ratio can provide a viable method for the measurement of Young's modulus and Poisson's ratio of elastic layers. After compression test of solid or annular disks of the same material but different aspect ratios, the effective moduli can be plotted against the known aspect ratios. Depending on the type of disks and the BCs, choosing the right equation out of Eqs. (52)–(55) for Γ to fit the data will yield both Young's modulus and Poisson's ratio of the material. There are two advantages of using this method: first, due to the sensitivity of effective modulus on Poisson's ratio, the measurement precision is expected to be high; second, Poisson's ratio can be measured without camera setup or the measurement of bulk modulus. This method is illustrated by using the experimental data provided in (Anderson et al., 2004). We use our analytical solution of effective modulus, Eq. (51) with Γ given by Eq. (52), to obtain ν by fitting the experimental $E_c/E \sim a/h$ data taken from (Anderson et al., 2004). The experimental data points and analytical fitting curves are drawn in Fig. 12. We find $\nu = 0.4995$ if fitting all six data points or $\nu = 0.49965$ if fitting the first five data points considering the equations are less accurate when $a/h > 25$. The Poisson's ratios found by our method are only slightly smaller compared to the experimentally measured $\nu = 0.4999$ out of bulk and Young's moduli.

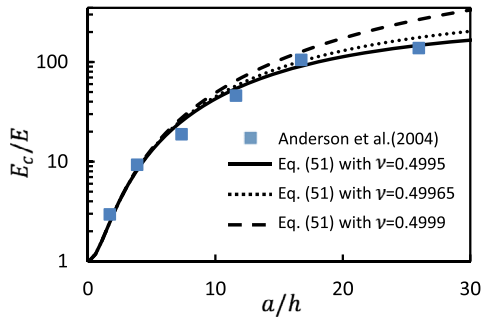

Fig. 12. Fitting the experimental data points of $E_c/E \sim a/h$ taken from (Anderson et al., 2004) by Eq. (51) can yield Poisson's ratio $\nu = 0.4995$ if all six data points are fitted or $\nu = 0.49965$ if only the first five data points are fitted, which are only slightly smaller than the experimentally measured $\nu = 0.4999$.

4.2. Incompressible material

With the solutions for elastically compressible layers, we are able to get specific solutions for incompressible materials by letting ν approach 0.5. Through the comparison between our degenerated solution and the incompressible elastic layer results reported by Gent and Lindley (1959), our solutions can be further double checked.

With

$$r_0 = \sqrt{\frac{3a^2b^2\left(a^2-b^2\right)}{\left(a^2-b^2\right)h^2 + 6a^2b^2\ln(a/b)'}} \tag{56}$$

being an intrinsic length scale of an annular disk with outer radius a, inner radius b and thickness h, we can obtain the following solutions of displacements, interfacial stresses and effective moduli for incompressible elastic layers: solid disks:

$$u_r^S = 3\left(1-\frac{z}{h}\right)\frac{z}{h}r\epsilon_0, \quad u_z^S = \frac{z^2}{h}\left(-3+2\frac{z}{h}\right)\epsilon_0 \tag{57}$$

$$\sigma_z^S/(E\epsilon_0) = -\left(\frac{a^2-r^2}{h^2}+\frac{2}{3}\right), \quad \tau_{rz}^S/(E\epsilon_0) = r/h \tag{58}$$

$$E_c^S/E = 1+2s^2 \text{ with shape factor } s = \frac{a}{2h} \text{ for solid disks} \tag{59}$$

annular disks:

$$u_r^A = 3\left(1-\frac{z}{h}\right)\frac{z}{h}\left(r-\frac{r_0^2}{r}\right)\epsilon_0, \quad u_z^A = \frac{z^2}{h}\left(-3+2\frac{z}{h}\right)\epsilon_0 \tag{60}$$

$$\begin{aligned}\sigma_z^A/(E\epsilon_0) &= 2\left[\frac{a^2\ln\left(\frac{a}{h}\right)-b^2\ln\left(\frac{b}{h}\right)}{a^2-b^2}-\ln\left(\frac{r}{h}\right)\right]\frac{r_0^2}{h^2}-\left(\frac{r^2-a^2-b^2}{h^2}+\frac{2}{3}\right)\\ \tau_{rz}^A/(E\epsilon_0) &= \left(r-\frac{r_0}{r}\right)/h\end{aligned} \tag{61}$$

$$E_c^A/E = 1+\frac{a^2+b^2-2r_0^2}{2h^2} \tag{62}$$

annular disks with rigid shaft:

$$u_r^{AR} = 3\left(1-\frac{z}{h}\right)\left(r-\frac{b^2}{r}\right)\frac{z}{h}\epsilon_0, u_z^{AR} = \left(\frac{z}{h}\right)^2\left(-3+2\frac{z}{h}\right)h\epsilon_0 \tag{63}$$

$$\begin{aligned}\sigma_z^{AR}/(E\epsilon_0) &= -\frac{2}{3}+\frac{r^2-a^2}{h^2}-\frac{b^2}{3a^2}-\frac{2b^2\ln(r/a)}{h^2}\\ \tau_{rz}^{AR}/(E\epsilon_0) &= \left(r-\frac{b^2}{r}\right)/h\end{aligned} \tag{64}$$

$$E_c^{AR}/E = 1+\frac{a^2-3b^2}{2h^2}+\frac{b^4}{h^2r_0^2} \tag{65}$$

Infinitely long strips:

$$u_x^I = 6x\left(1-\frac{z}{h}\right)\frac{z}{h}\epsilon_0, \quad u_z^I = \left(\frac{z}{h}\right)^2\left(-3+2\frac{z}{h}\right)h\epsilon_0 \tag{66}$$

$$\sigma_z^I/(E\epsilon_0) = -1+2\frac{x^2-a^2}{h^2}, \quad \tau_{xz}^I/(E\epsilon_0) = \frac{2x}{h} \tag{67}$$

$$E_c^I/E = \frac{4}{3}(1+s^2) \text{ with shape factor } s=\frac{a}{h} \text{ for infinite long strips} \tag{68}$$

The maximum bulging displacement of incompressible solid disks can be obtained by setting $z = h/2$ in the first equation of Eq. (57):

$$u_r^S(a,h/2) = 3\epsilon_0 a/4 \tag{69}$$

which is the same as what (Thornton et al., 1988) has reported. Moreover, the interfacial shear stress given by the second equations of Eqs. (58) and (67) and the effective moduli given by Eqs. (59) and (68) have exactly the same form as (Gent and Lindley, 1959) which were solved using "pressure method" and validated by experiments in the same paper, while the interfacial normal stress given by the first equation of Eq. (58) has a slight difference from what Gent has obtained ($\sigma_{Gent}/E\epsilon_0 = -(a^2-r^2)/h^2-1$) which was validated experimentally in (Gent et al., 1974), but this difference is negligible when the aspect ratio is large. As another example, Eq. (62) is the same as the result from (Tsai, 2012) even though Tsai assumed parabolic bulging profile. In summary, our solutions for elastically compressible solid and annular disks as well as infinitely long strips can successfully decay to existing solutions of incompressible disks and our solutions for annular disks with rigid shaft is the first of its kind.

5. Conclusions

Based on variable separation, analytical solutions to the displacement filed, stress field as well as effective modulus are analytically derived for elastically compressible layers perfectly bonded between parallel rigid plates. Without adopting the conventional assumptions used in pressure method, the displacement solutions we find can exactly satisfy the equilibrium equations and all essential BCs, and weakly satisfy the natural BCs. Following the same process, we have achieved closed-form solutions for elastically compressible annular disks with and without a rigid frictionless shaft as well as infinitely long strips. All of our analytical solutions have found excellent agreement with FEM results over a wide range of Poisson's ratio, aspect ratio ($1 < a/h < 25$) and radius ratio. Displacement, stress and effective modulus all become extremely sensitive when Poisson's ratio is close to 0.5, i.e. the material is almost incompressible. With the analytical expressions of effective modulus, the Young's modulus and Poisson's ratio can be experimentally acquired by fitting the $E_c/E \sim a/h$ curve obtained through a series of compression tests without any camera setup. We have also validated that our generic solutions can successfully degenerate into specific cases.

Acknowledgments

This work is supported by the NSF NASCENT (Nanomanufacturing Systems for Mobile Computing and Mobile Energy Technologies) Center under Grant No. 1160494 and the NSF CMMI award under Grant No. 1301335. S. Q. acknowledges the Eugene A. Ripperge endowed graduate fellowship.

Appendix A. Discussion of the sign of λ

In Section 2.2, we have obtained a displacement solution which can exactly satisfy both equilibrium equations, all the essential BCs as well as the weak form of the traction-free condition on the sidewall. During the analysis, we assume λ to be positive and neglect other possibilities. When λ is zero or negative, other solutions may exist, but we are going to prove that these are not valid solutions to our problem.

Back to Eq. (10), if we choose λ to be negative and set

$$-\frac{\beta^2}{h^2} = \frac{1-2\nu}{1-\nu}\lambda \tag{A1}$$

Following similar steps in Section 2.2, another solution can be reached as:

$$\begin{aligned} u_r^S &= \bar{A}_1 G_{1+} J_1(\beta r/h) \\ u_z^S &= \bar{A}_1 \coth(\beta/2) G_{1-} J_0(\beta r/h) - \varepsilon_0 z \end{aligned} \tag{A2}$$

where

$$G_{1\pm} = \sinh(\beta z/h)(1-z/h) \pm \sinh(\beta(1-z/h))(z/h) \tag{A3}$$

with J_i being the ith order of Bessel function of the first kind. Similarly, the unknown coefficient $\bar{A}_1$ can be determined through the traction-free BC ($\langle\sigma_r\rangle|_{r=a} = 0$) as

$$\bar{A}_1 = \frac{\nu(3-4\nu)\epsilon_0 h}{4(1-2\nu)\bar{Q}_1} \tag{A4}$$

where $\bar{Q}_1 = [J_0(\bar{\omega}) - (1-2\nu)J_2(\bar{\omega})]/2$ and $\bar{\omega} = \beta a/h$. However, when solving the consequent eigenvalue problem like Eqs. (17)–(19), the corresponding relation between Poisson's ratio and β turns out to be

$$\beta = (4-3\nu)\sinh(\beta) \tag{A5}$$

from which it is possible for us to find a non-zero β only when physically impossible values of Poisson's ratio, i.e. $\nu > 0.5$, is used.

Another possible value for λ is zero and this special case yields a displacement field

$$u_r^S = 0 \quad \text{and} \quad u_z^S = -\epsilon_0 z \tag{A6}$$

which is only appropriate for material with zero Poisson's ratio.

With above discussions, we have proved that it is legitimate to assume λ to be positive in Section 2.2.

References

Al-Chalabi, M., Huang, C., 1974. Stress distribution within circular cylinders in compression. Int. J. Rock Mech. Mining Sci. Geomech. Abstr., 45–56, Elsevier
Al-Chalabi, M., McCormick, F., Huang, C., 1974. Strain distribution within compressed circular cylinders. Exp. Mech. 14, 497–501.
Anderson, M., Mott, P., Roland, C., 2004. The compression of bonded rubber disks. Rubber Chem. Technol. 77, 293–302.
Brady, B., 1971a. Effects of inserts on the elastic behavior of cylindrical materials loaded between rough end-plates. Int. J. Rock Mech. Mining Sci. Geomech. Abstr., 357–369, Elsevier
Brady, B., 1971b. An exact solution to the radially end-constrained circular cylinder under triaxial loading. Int. J. Rock Mech. Mining Sci. Geomech. Abstr., 165–178, Elsevier
Chalhoub, M.S., Kelly, J.M., 1990. Effect of bulk compressibility on the stiffness of cylindrical base isolation bearings. Int. J. Solids Struct. 26, 743–760.
Chalhoub, M.S., Kelly, J.M., 1991. Analysis of infinite-strip-shaped base isolator with elastomer bulk compression. J. Eng. Mech. 117, 1791–1805.
Gent, A., Lindley, P., 1959. The compression of bonded rubber blocks. Proc. Inst. Mech. Eng. 173, 111–122.
Gent, A.N., Meinecke, E.A., 1970. Compression, bending, and shear of bonded rubber blocks. Polym. Eng. Sci. 10, 48–53.
Gent, A., Henry, R., Roxbury, M., 1974. Interfacial stresses for bonded rubber blocks in compression and shear. J. Appl. Mech. 41, 855.
Horton, J., Tupholme, G., Gover, M., 2002. Axial loading of bonded rubber blocks. J. Appl. Mech. 69, 836–843.
Horton, J.M., Tupholme, G.E., Gover, M.J.C., 2003. Axial loading of annular bonded rubber blocks. Rubber Chem. Technol. 76, 1194–1211.
Imbimbo, M., De Luca, A., 1998. F.E. stress analysis of rubber bearings under axial loads. Comput. Struct. 68, 31–39.
Kakavas, P., 1997. Fracture analysis of bonded elastomeric disks subjected to triaxial stress. J. Appl. Polym. Sci. 65, 1821–1827.

Khang, D.Y., Jiang, H.Q., Huang, Y., Rogers, J.A., 2006. A stretchable form of single-crystal silicon for high-performance electronics on rubber substrates. Science 311, 208–212.
Kim, D.H., Ahn, J.H., Choi, W.M., Kim, H.S., Kim, T.H., Song, J.Z., Huang, Y.G.Y., Liu, Z.J., Lu, C., Rogers, J.A., 2008. Stretchable and foldable silicon integrated circuits. Science 320, 507–511.
Koh, C.G., Kelly, J.M., 1989. Compression stiffness of bonded square layers of nearly incompressible material. Eng. Struct. 11, 9–15.
Koh, C.G., Lim, H.L., 2001. Analytical solution for compression stiffness of bonded rectangular layers. Int. J. Solids Struct. 38, 445–455.
Lee, C.H., Kim, D.R., Zheng, X., 2010. Fabricating nanowire devices on diverse substrates by simple transfer-printing methods. Proc. Nat. Acad. Sci. 107, 9950–9955.
Mott, P.H., Roland, C.M., 1995. Uniaxial deformation of rubber cylinders. Rubber Chem. Technol. 68, 739–745.
Pinarbasi, S., Akyuz, U., Mengi, Y., 2006. A new formulation for the analysis of elastic layers bonded to rigid surfaces. Int. J. Solids Struct. 43, 4271–4296.
Pinarbasi, S., Mengi, Y., Akyuz, U., 2008. Compression of solid and annular circular discs bonded to rigid surfaces. Int. J. Solids Struct. 45, 4543–4561.
Sakai, E., 1995. Measurement and visualization of the contact pressure distribution of rubber disks and tires. Tire Sci. Technol. 23, 238–255.
Suh, J.B., 2007. Stress analysis of rubber blocks under vertical loading and shear loading. University of Akron.
Thornton, J., Montgomery, R., Thompson, C., Dillard, D., 1988. Analysis of interfacial stresses for elastomeric disks in compression. Polym. Eng. Sci. 28, 655–659.
Tsai, H.-C., 2005. Compression analysis of rectangular elastic layers bonded between rigid plates. Int. J. Solids Struct. 42, 3395–3410.
Tsai, H.-C., 2012. Compression behavior of annular elastic layers bonded between rigid plates. J. Mech. 1, 1–7.
Tsai, H.-C., Lee, C.-C., 1998. Compressive stiffness of elastic layers bonded between rigid plates. Int. J. Solids Struct. 35, 3053–3069.
Williams, M.L., Blatz, P., Schapery, R.A., 1961. Fundamental studies relating to systems analysis of solid propellants. DTIC Document.
Wilson, D., Stenzenberger, H.D., Hergenrother, P.M. (Eds.), 1990. Polyimides. Blackie, Chapman and Hall, USA, New York.
Wypych, G., 2012. PDMS polydimethylsiloxane. In: Wypych, G. (Ed.), Handbook of Polymers. Elsevier, Oxford, pp. 328–332.
Yeoh, O., Pinter, G., Banks, H., 2002. Compression of bonded rubber blocks. Rubber Chem. Technol. 75, 549–562.
Zhao, X.H., Huebsch, N., Mooney, D.J., Suo, Z.G., 2010. Stress-relaxation behavior in gels with ionic and covalent crosslinks. J. Appl. Phys. 107.